CFD Validation Study of a Hypersonic Cone-Slice-Flap Variable Geometry Configuration

Laura M. White,* Thomas K. West IV,† Matthew N. Rhode,‡ and Elizabeth F. Rieken, §
NASA Langley Research Center, Hampton, VA 23681

Jacob J. Lampenfield¶ and Daniel A. Rodriguez‖
Analytical Mechanics Associates Inc. at NASA Langley Research Center, Hampton, VA 23681

Model validation is the process of determining the degree of accuracy between physical reality and the model. The result of model validation can either be used to improve the model through calibration or quantify the model-form uncertainty. This work focuses on providing the model-form uncertainty through an area metric for a hypersonic cone-slice-flap variable geometry configuration given uncertainty in both the simulation and experimental data. The research here compares two different turbulence models for the simulations. For a variable geometry, performing uncertainty quantification to capture the model-form uncertainty on every configuration is computationally challenging. This work lays out a procedure that can give an accurate representation of the model-form uncertainty using a small number of high-fidelity runs and many low-fidelity runs on multiple configurations. Running this comparison provides a quantifiable measurement for the accuracy of each turbulence model for this type of design. The high-fidelity CFD solver used was VULCAN-CFD and the low-fidelity results came from Cart3D. The experimental data came from the 20-Inch Mach 6 Tunnel located at NASA Langley Research Center. The present work showed that the using both the Spalart and Allamaras and Menter Shear-Stress Transport turbulence models overpredicted the drag and lift coefficient, while underpredicting the pitching moment coefficient. The model-form uncertainty estimate resulted in up to a 13.6% change in the total uncertainty for the drag coefficient, up to a 57.4% change in total uncertainty for the lift coefficient, and up to a 100% change in total uncertainty for the pitching moment coefficient.

Nomenclature

a_i	coefficient for ith basis function	N_t	number of terms
C	coefficient	n	number of random variables
C_D	drag coefficient	p	order-of-accuracy
C_L	lift coefficient	q	order of polynomial
C_M	pitching moment coefficient	U	uncertainty
$\mathbf{D}$	deterministic variables	U^g	grid error uncertainty
d_L	left area metric	Re	Reynolds number
d_R	right area metric	R_b	model base radius (in.)
$E(x)$	experimental CDF at x	R_n	nose radius (in.)
$F(x)$	simulation CDF at x	SA	Spalart and Allmaras turbulence model
$g_L(x)$	left CDF distribution	S_{ref}	model reference area (in.^{2})
$g_R(x)$	right CDF distribution	SST	Menter Shear-Stress Transport model
h	Gaussian process fit model	Y	arbitrary quantity of interest
L	model length (in.)	y^+	dimensionless wall distance
M	Mach number	X_f	flap leading edge location (in.)

*Aerospace Engineer, Aeronautics Systems Analysis Branch, Systems Analysis and Concepts Directorate, Member AIAA
†Aerospace Engineer, Vehicle Analysis Branch, Systems Analysis and Concepts Directorate, Senior Member AIAA.
‡Aerospace Engineer, Aerothermodynamics Branch, Research Directorate, Senior Member AIAA.
§Complex Systems Engineer, Engineering Integration Branch, Engineering Directorate, Member AIAA.
¶Research Engineer, Hypersonic Airbreathing Propulsion Branch, Research Directorate, Member AIAA
‖Research Engineer, Hypersonic Airbreathing Propulsion Branch, Research Directorate

X_s	slice leading edge location (in.)
α	angle of attack (deg)
γ	ratio of specific heats
κ	Von Kármán's constant
Ψ_i	basis function representing ith mode
σ, c_{w2}	SA model closure coefficients
σ_{w1}, σ_{w2}	SST model closure coefficients
θ_f	flap deflection angle (deg)
ξ	standard random variable

Subscripts

L	left
R	right
SA	aligns with SA turbulence model
SST	aligns with SST model

Superscripts

$Cart3D$	aligns with Cart3D simulation
$full$	aligns with the final uncertainty
$lower$	lower uncertainty bound
$nominal$	aligns with nominal value
$upper$	upper uncertainty bound
$Vulcan$	aligns with VULCAN-CFD simulation

I. Introduction

Validation is the process of determining the degree to which a model or simulation is an accurate representation for the real world within its intended application, whereas verification is the process determining the extent to which an model and simulation is compliant with its requirements and specifications as detailed in it conceptual models, mathematical model, or other constructs [1]. One approach to validation is to compare verified numerical solutions with experimental data for which uncertainty is estimated in both the computational model and experimental data. Including uncertainty in both experimental data and simulation provides a statistical-based measurement of the model-form uncertainty. For a variable geometry configuration, performing uncertainty quantification on the simulation of every geometric arrangement and directly computing the disagreement with the experimental measurements would be particularly challenging due to the considerable number of computational resources needed for such a study.

The goal of the current work is to present a validation procedure for a variable geometry configuration, with limited computational resources and numerous sources of uncertainty in the experimental and simulation data. The cone-slice-flap configuration can be seen in Fig. 1. Previous research has been conducted on similar geometries. [2–5] However, these studies do not consider multiple turbulence models, flow solvers, and uncertainty sources. Roy et al. [2, 3] investigated a variable geometry, albeit with less geometrical parameter variation then what is considered in this work. The proposed validation procedure includes the use of a multifidelity approach to characterize the configuration geometric space. Additionally, a non-intrusive polynomial chaos surrogate model is used to reduce the computational burden of forward uncertainty propagation [6].

The cone-slice-flap model was studied experimentally at the 20-Inch Mach 6 Tunnel facility located at NASA Langley Research Center [7]. The experimental database consisted of force and moment data and stagnation pressure data measured in a port at the nose of the model. Simulations were performed as three dimensional (3D), calorically perfect gas flow with a state-of-the-art Reynolds Averaged Navier Stokes (RANS) computational fluid dynamic (CFD) solver employing two turbulence models. These cases were computed with flow conditions that consisted of unit Reynolds numbers of 2.5 million/ft and 4 million/ft. An inviscid solver is also considered to enable the multifidelity analysis approach. Previous work done by White et al. [8], which looked at the same wind tunnel model and experiments for a single configuration, is leveraged here. Aspects of this previous work, including grid convergence studies of the CFD models and the experimental uncertainty quantification approach, were carried forward into the present study.

This paper is organized to first present the experimental test that was performed and uncertainty sources in the following Section II. Section III presents the computational models, initial configuration study, and corresponding uncertainty sources in the computational models. Section IV presents the uncertainty quantification methodology and the validation approach when comparing the 20-Inch Mach 6 Wind Tunnel data and CFD uncertainty results. The results and important findings are discussed in Section V. Finally, the concluding remarks are discussed in Section VI.

II. Experimental Test

An experiment was conducted in the NASA Langley 20-Inch Mach 6 Tunnel to investigate the aerodynamic characteristics of a cone-slice-flap configuration. The stainless-steel wind tunnel model was a 7-deg half-angle spherically blunted cone measuring 12 inches in length from the virtual sharp cone tip to the base and featured a

sliced surface parallel to the centerline axis along with a flap mounted on the slice surface. An illustration of a model configuration on a sting support is shown in Fig. 1, in an inverted orientation.

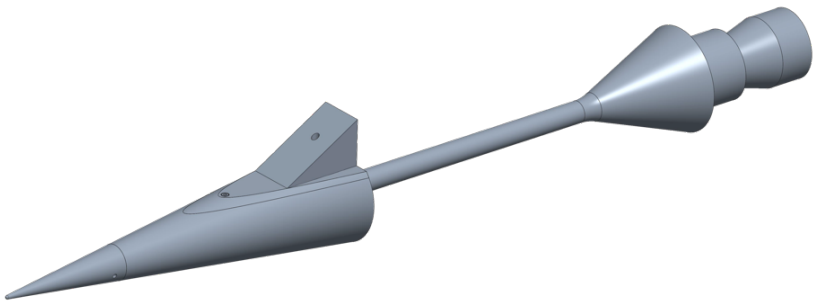

Fig. 1 Cone-Slice-Flap wind tunnel model (shown inverted).

The model was designed with several interchangeable parts to investigate the aerodynamic effects of nose radius (R_n/R_b), slice leading edge location (X_s/L), flap leading edge location (X_f/L), and flap deflection angle in degrees (θ_f), with the slice and flap leading edge locations normalized by the model length, $L = 12$ in., and the nose radius normalized by the model base radius, $R_b = 1.4734$ inches. In total, there were five flap deflection angles, five different flap leading edge locations, four different planar slice leading edge locations, and four different nose cone radii. These configurations were interchanged for each experimental run and tested at various wind tunnel conditions. The experimental model consisted of 33 different combinations of these parameters. The geometric parameters for each configuration tested are given in Table 1. An exploded view of the model parts is shown in Fig. 2. The run matrix corresponding to the cases used in the validation work of this paper is located in Table A1 in the Appendix.

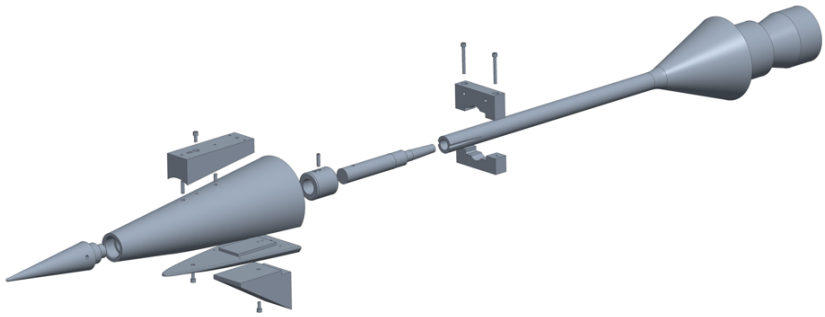

Fig. 2 Exploded view of cone-slice-flap wind tunnel model.

A minimum nose radius was specified for the model so that a small pressure orifice could be installed in the blunted nose. This orifice was used to obtain post-normal-shock stagnation pressure measurements at zero angle of attack so that the Mach number at the model location in the test section could be determined directly for subsequent calculations of the flow conditions. The model was sting-mounted through the base on a six-component force balance equipped with a water-cooling jacket to regulate the balance temperatures in the high-temperature hypersonic flow. Base pressure was measured using two flush orifices on the model base. The model was tested over an angle of attack range from -4° to $+12^\circ$ and at unit Reynolds numbers from 1.0 million/ft to 4.0 million/ft.

Table 1 Geometrical parameters of each configuration

Configuration	R_n/R_b	X_s/L	X_f/L	θ_f (deg)
1	0.04	0.65	-	0
2	0.04	0.65	0.80	30
3	0.04	0.65	0.85	15
4	0.04	0.65	0.90	30
5	0.04	0.70	-	0
6	0.04	0.70	0.85	30
7	0.04	0.75	-	0
8	0.04	0.75	0.80	30
9	0.04	0.75	0.90	15
10	0.15	0.65	0.85	15
11	0.15	0.70	0.80	15
12	0.15	0.70	-	0
13	0.15	0.70	0.90	15
14	0.15	0.70	0.90	30
15	0.15	0.75	-	0
16	0.15	0.75	0.85	15
17	0.15	0.75	0.85	30
18	0.30	0.65	-	0
19	0.30	0.65	0.80	30
20	0.30	0.65	0.90	30
21	0.30	0.70	0.85	15
22	0.30	0.75	-	0
23	0.30	0.75	0.80	30
24	0.30	0.75	0.90	30
25	0.04	0.72	0.83	7
26	0.04	0.72	0.83	24
27	0.21	0.72	0.83	7
28	0.21	0.72	0.83	24
29	0.15	0.72	0.88	7
30	0.15	0.72	0.88	24
31	0.21	0.72	0.88	7
32	0.21	0.72	0.88	24
33	0.15	0.70	0.85	15

Uncertainty sources for the experimental measurements were defined in White et al. [8], which include both aleatory and epistemic uncertainties to describe the systematic and random error in the measurements. The experimental uncertainties consisted of calibration uncertainties, settling chamber uncertainties, model nose pressure uncertainty, and transfer distances of the systematic error. Random error is assessed within the wind tunnel by looking at the spread in repeated runs. For more details regarding the experimental measurement uncertainty refer to White et al. [8].

The uncertainty quantification procedure described by White et al. [8] was employed for each configuration to capture the 95% experimental uncertainty intervals. The experimental uncertainty for configuration 33 can be seen in Table 2. Note that the experimental uncertainty is a function of the tested conditions. This uncertainty evaluated here was used to produce a validation metric for each configuration, shown in Section IV.C.

III. Flow Solvers

For this work, a viscous CFD solver developed at NASA Langley Research Center, Viscous Upwind Algorithm for Complex Flow Analysis (VULCAN-CFD) [9], was used. VULCAN-CFD is a turbulent, non-equilibrium, finite-rate chemical kinetics, Navier-Stokes flow solver for either structured, cell-centered, multi-block grids or fully unstructured grids. The work here also leveraged the inviscid solver Cart3D [10] with adjoint-based grid refinement, which was developed at NASA Ames Research Center. Cart3D is a scalable, multi-level, linearly-exact upwind solver that uses domain decomposition to achieve scalability for both steady and time-dependent flows [10]. Within VULCAN-CFD, two turbulence models were investigated: the one-equation Spalart-Allmaras (SA) model [11] and the two-equation Menter Shear-Stress Transport (SST) model [12]. In the remainder of this section, geometry modeling assumptions and grid convergence studies with the RANS CFD calculations are discussed, followed by a listing of uncertainty sources considered in the modeling.

Table 2 Configuration 33 95% probability range for the wind tunnel load

α	Uncertainty Variable	WT Reading	95% Uncertainty Range
-4°	C_D	0.1069	[0.1051,0.1092]
	C_L	-0.1118	[-0.1146,-0.1104]
	C_M	-0.0237	[-0.0252,-0.0233]
0°	C_D	0.0958	[0.0938,0.0977]
	C_L	0.0101	[0.0084,0.0125]
	C_M	-0.0083	[-0.0092,-0.0074]
4°	C_D	0.1172	[0.1153,0.1193]
	C_L	0.1379	[0.1361,0.1403]
	C_M	-0.0020	[-0.0032,-0.0013]
12°	C_D	0.2558	[0.2541,0.2585]
	C_L	0.4547	[0.4530,0.4581]
	C_M	0.0303	[0.0294,0.0316]

A. Geometry Modeling Assumptions

The computational models included a sting attached to the base of the cone-slice-flap geometry to account for sting effects within the wind tunnel data. A VULCAN-CFD analysis was conducted at multiple wind tunnel representative conditions to determine where the sting could be truncated and to minimize the computational burden of modeling the entire sting hardware. This analysis showed a sting length of approximately 6 in. aft from the model base could be used in CFD calculations, which resulted in less than 0.1% change in the loads. For reference, the wind tunnel model sting length was, in total, 8.5 in. from the base of the model to the wind tunnel attachment point. Neither the wind tunnel walls, nor the model support system were modeled [13]. Using the model geometry, tunnel geometry, and knowledge of the freestream Mach number, isentropic and oblique shock relations predicted that no reflected shocks would impinge on the model or sting. Additionally, the model was deemed small enough in diameter to remain outside the tunnel wall boundary layer, based on years of previous testing. All of the CFD results presented have the same reference area of 6.8202 in.^{2} and reference length of 2.9468 in.

White et al. [8] preformed a grid convergence study on configuration 33, which is in the center of the geometric space. The grid error for the viscous simulations and Cart3D at configuration 33 can be seen in Table 3. Details regarding how the grid convergence study was performed for each solver are shown in White et al. [8] The design point for the grid convergence study was determined such that it has the potential for the highest uncertainty. This grid error analysis was conducted at the highest angle of attack seen in the wind tunnel, angle of attack of 12°, and largest nominal Reynolds number of 4.0 million/ft. These conditions were chosen because they represent a case that would require high grid resolution and, therefore, yield the largest grid error for a fixed grid. This grid error was used for each configuration analyzed with VULCAN-CFD. For Cart3D, the grid uncertainty was determined for each configuration using the error computed from the adjoint solution-based grid refinement. Note that the moment uncertainty is higher due to its value being close to zero.

Table 3 Configuration 33 grid uncertainty results

	$U^g_{C_L}$	$U^g_{C_D}$	$U^g_{C_M}$
Viscous Solvers	± 2.24%	± 0.74%	± 17.70%
Cart3D	± 0.08%	± 0.14%	± 13.2%

B. Configuration Study

Six configurations are studied here using the high-fidelity viscous flow solver, VULCAN-CFD; the configurations and boundary conditions are listed in Table 4. For each configuration, VULCAN-CFD used a cold wall boundary condition of 80°F (539.67 R) and assumed a calorically perfect gas model with a ratio of specific heats, γ =1.4. These configurations were chosen for the high-fidelity analysis given their spread across the design space and the variety of predicted aerodynamic flow features. To quantify the turbulence parameter uncertainty, selected angles of attack on each configuration were chosen for a turbulence parameter uncertainty quantification (UQ) study at nominal wind tunnel conditions; these are circled in Table 4. The low-fidelity solver, Cart3D, was run for every configuration. The VULCAN-CFD results were also used for anchoring the drag coefficient from Cart3D. Four angles of attack, $-4°, 0°, 4°$, and $12°$, were used for anchoring points. Conducting the analysis at four angles of attack helps capture the trends of the loads on the configuration space and test conditions space for anchoring with the low-fidelity flow solver. The anchoring methodology is given in detail in Section III.C.

Table 4 Parameter variation and flow solver conditions for the anchoring and UQ analysis. The circled values represent the cases used for the turbulence parameter UQ study

Configuration	X_f/L	X_s/L	R_n/R_b	θ_f	M	Angle of Attack	Reynolds Number	Total Temperature
1	-	0.65	0.04	0°	5.88	-4°	3,962,576.17/ft	872.26 R
						0°	3,946,004.98/ft	873.44 R
						4°	3,954,795.36/ft	873.39 R
						(12°)	3,944,422.22/ft	873.90 R
8	0.80	0.75	0.04	30°	5.94	-4°	3,998,002.04/ft	872.39 R
						0°	3,991,847.14/ft	871.60 R
						4°	3,993,048.52/ft	871.96 R
						(12°)	3,993,300.00/ft	871.16 R
10	0.85	0.65	0.15	15°	5.93	(-4°)	2,635,724.15/ft	861.51 R
						0°	2,616,303.65/ft	861.58 R
						4°	2,613,524.06/ft	862.01 R
						12°	2,621,850.00/ft	861.14 R
13	0.90	0.70	0.15	15°	5.97	(-4°)	4,005,678.88/ft	865.88 R
						0°	3,984,021.08/ft	863.41 R
						4°	3,989,582.28/ft	865.02 R
						12°	3,991,251.85/ft	865.80 R
19	0.80	0.65	0.30	30°	5.97	-4°	4,018,200.00/ft	865.17 R
						(0°)	4,003,800.00/ft	864.78 R
						4°	4,010,812.40/ft	864.71 R
						12°	4,001,862.50/ft	865.56 R
22	-	0.75	0.30	0°	5.96	-4°	4,065,020.99/ft	868.14 R
						0°	4,072,734.76/ft	862.83 R
						(4°)	4,066,312.38/ft	865.12 R
						12°	4,063,550.00/ft	864.91 R
25	0.83	0.72	0.04	7°	5.95	-4°	2,761,728.51/ft	864.70 R
						(0°)	2,760,282.39/ft	866.55 R
						4°	2,760,774.83/ft	865.68 R
						12°	2,758,403.70/ft	867.00 R
33	0.85	0.70	0.15	15°	5.94	-4°	2,600,200.00/ft	862.04 R
						0°	2,605,900.00/ft	861.63 R
						(4°)	2,600,100.00/ft	863.59 R
						12°	2,602,800.00/ft	864.08 R

For VULCAN-CFD, the RANS equations were solved with a second-order central differencing scheme for the viscous terms. The inviscid flux scheme used was the Edwards low-diffusion flux-splitting scheme [14] with a third-order upwind-based monotone upwind schemes for scalar conservation laws (MUSCL) reconstruction scheme and the van Leer limiter. Grid wall spacing was selected such that the nominal y^+ was 0.5. Near separation regions and sharp edges, the maximum y^+ was 3.8. The Courant Friedrichs Lewy (CFL) number started at 0.1 and was increased up to 50, where it was held until no noticeable changes occurred over 5,000 iterations in the L^2 norm, mass flow rate error, and loads. Time integration was done via an incomplete lower-upper (LU) factorization scheme. The grid used for VULCAN-CFD was the medium grid that was described by White et al. [8].

The wind tunnel conditions for each solver in the UQ study and the wind tunnel data are in Table 4. Because wind tunnel measurements are not obtained at the exact angle of attack of interest, the intermediate loads at a particular angle of attack were determined by linearly interpolating the wind tunnel load readings around the angle of attack of interest. Linear interpolation was used because the data were acquired at 20 samples/s while continually pitching the model at 1 deg/s. The combination of 20 samples/s and a pitch rate of 1 deg/s result in a data sample every 0.05 degrees; therefore, linear interpolation should yield accurate results.

Cart3D uses a cell-centered finite-volume upwind differencing scheme with Cartesian meshes. For this work, Cart3D adjoint-based mesh refinement was used to minimize the discretization errors. The analysis was done on a half-body with Riemann boundary conditions, and nine adaption cycles were performed. Cart3D cases were run on each of the 33 configurations. The loads predicted by Cart3D were corrected based on the differences with the viscous solutions, which is described in the next section.

C. Low-Fidelity Anchoring Approach

To account for the discrepancy between the low-fidelity model (Cart3D) and high-fidelity model (VULCAN-CFD), an anchoring approach was used on the low-fidelity predictions. The lift and moment coefficients from Cart3D lie within the grid uncertainty error of the VULCAN-CFD data, but the drag coefficient does not for each configuration, as shown in Fig. 3 for configuration 2. Given this, the anchoring approach is only applied to the drag coefficient to ensure there is no double counting of uncertainty with this method.

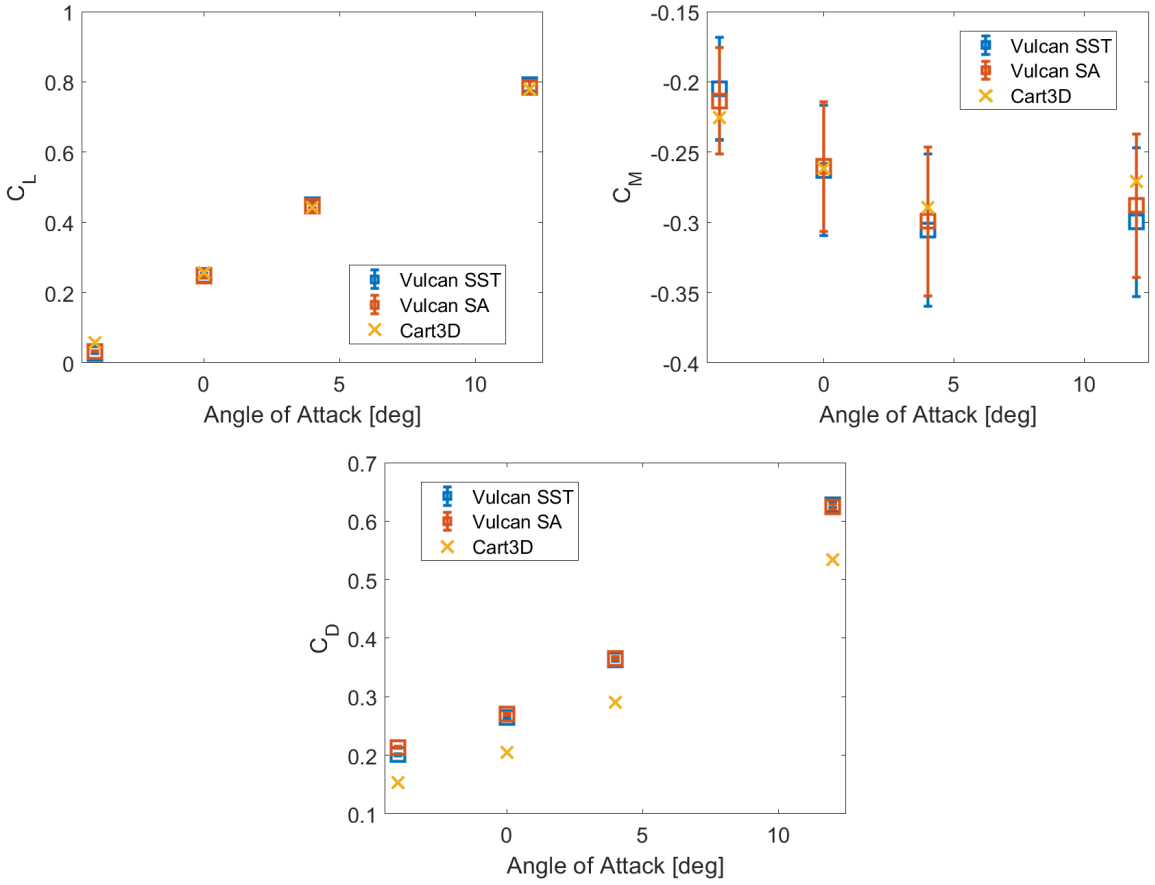

Fig. 3 The lift, moment, and drag coefficients for VULCAN-CFD and Cart3D with grid error included in the VULCAN-CFD for Configuration 2.

The anchoring approach used a Gaussian process model to account for the geometric configuration and Reynolds number variations. Gaussian process models have been used heavily throughout the literature for prediction on expensive simulations [15–18]. A Gaussian process model was built using the MATLAB fit Gaussian process function that

applied the squared exponential function as the kernel and used the default optimizer for the hyperparameters: sigma, kernel scale, and standardization [19]. The Gaussian process model was fit using the delta between VULCAN-CFD and Cart3D drag coefficients, denoted by $h_{C_D,m}$ and represented in Eq. (1). The anchoring approach was conducted on both SA and SST turbulence models.

$$h_{C_D,m}\left(\frac{R_n}{R_b}, \frac{X_s}{L}, \frac{X_f}{L}, \theta_f, Re, \alpha\right) \approx C_{D,m}^{Vulcan} - C_D^{Cart3D} \tag{1}$$

Here, $m \in$ {SA,SST}, $\frac{R_n}{R_b}$, $\frac{X_s}{L}$, $\frac{X_f}{L}$, and θ_f represent the geometrical variables described in Table 1, and C_D^{Vulcan}, C_D^{Cart3D}, Re, and α represent the drag coefficient for VULCAN-CFD, drag coefficient for Cart3D, Reynolds number, and angle of attack, respectively. The geometric configurations, Reynolds number, and angles of attack used to fit the model can be seen in Table 4. This leads to the final drag coefficient for Cart3D being represented by Eq. (2). Notice that Eq. (2) is equal to the high-fidelity simulation when a configuration from the high-fidelity analysis is evaluated, because the Gaussian process model built here interpolates through the data used to build the model.

$$C_{D,m} = C_D^{Cart3D} + h_{C_D,m}\left(\frac{R_n}{R_b}, \frac{X_s}{L}, \frac{X_f}{L}, \theta_f, Re, \alpha\right) \tag{2}$$

To verify the Gaussian process, a leave-one-out cross validation (LOOCV) method was performed on the Gaussian process model that was built on the high-fidelity solutions [20]. LOOCV has been used throughout the literature to verify surrogate modeling and ensure that the model is a good fit for the data [21–24]. The LOOCV method takes the training input data set, leaves one sample out, and then builds a surrogate on the remaining data. After that a difference is computed between the predicted value and true value at the sample point left out. The process is repeated for each sample in the initial training data set and the mean square error is computed for each predicted versus true value. The LOOCV errors were 3.2358×10^{-5} and 2.8139×10^{-5} for the SST and SA Gaussian process models, respectively. Both errors are sufficiently small, thereby showing that the Gaussian process models built for the additive factor for the Cart3D drag data were an acceptable fit.

To verify the overall anchoring approach, Eq. (2) was constructed leaving out configuration 25. This configuration was chosen as the verification case because its geometrical configuration values lie in between the other fixed geometries. Configuration 25 also has an off-nominal Reynolds number of 2.7 million/ft. Table 5 shows the predicted values from Eq. (2), true VULCAN-CFD values, the differences, and the percent error between the VULCAN-CFD SA and SST drag coefficient results and predicted result from Eq. (2) at four angles of attack. All errors in the table are less than 5% and the absolute differences are less than 0.005. This shows that the anchoring approach does an adequate job of predicting the VULCAN-CFD drag coefficient. For the remaining results in this paper, configuration 25 is included in the training data unless stated otherwise.

Table 5 Verification of Eq. (2) with configuration 25

α	Eq. (2) SST	Eq. (2) SA	Vulcan SST C_D	Vulcan SA C_D	SST Diff.	SA Diff.	% Error SST	% Error SA
-4°	0.1138	0.1159	0.1175	0.1197	0.0037	0.0038	3.14 %	3.14 %
0°	0.0967	0.1039	0.1013	0.1019	0.0046	-0.0020	4.51 %	1.96 %
4°	0.1083	0.1095	0.1133	0.1145	0.0050	0.0050	4.37 %	4.34 %
12°	0.2189	0.2183	0.2165	0.2197	-0.0025	0.0014	1.15 %	0.64 %

D. Uncertainty Sources

This work considers two types of uncertainties: epistemic and aleatory uncertainty. Epistemic uncertainty is due to lack of knowledge or incomplete information, whereas aleatory uncertainty refers to uncertainty due to inherent variability. The rest of this section describes all the uncertainty sources considered and their justification.

Uncertainty sources in the closure coefficients for the two turbulence models were considered in this study. The uncertainties in the closure coefficients of both the SA and SST models have been studied throughout the literature to assess simulation uncertainty [25–28]. Uncertainty in the closure coefficients is inherently epistemic due to the lack of knowledge of turbulence in the flow. Key uncertainty sources identified by Erb et al. were selected for consideration in this study [25]. These uncertainties were assessed to determine the sensitivities of the various closure coefficients in

SA and SST models. The analysis conducted by Erb et al. was used due to its similarity to this study in geometry and freestream Mach number.

For the SA model, the closure coefficients σ, κ, and c_{w2} were varied; for more details on the model, refer to Spalart and Allmaras [11]. For the SST model, the closure coefficients σ_{w1}, σ_{w2}, and κ were varied; for more detail on the model, refer to Menter [12]. Descriptions of each closure coefficient can be seen in Table 6. The three uncertainty parameters were chosen such that they contribute at least 90% to the overall variance in the loads from the study done by Erb et al. [25]. Given the similarity between this work and that of Erb et al., this work assumed these closure coefficients will have a similar contribution to the overall uncertainty. Previous work by Schafer et al. [27] gives lower and upper bounds for each of these uncertain variables in each model, which can be seen in Table 6.

Table 6 Uncertainty sources for the CFD models

Uncertainty Variable	Description	Classification	Lower Bound	Upper Bound
κ	Von Kármán's constant	epistemic	0.38	0.42
SA Model				
σ	Turbulent Prandtl number	epistemic	0.6	1.0
c_{w2}	Part of g function	epistemic	0.055	0.3525
SST Model				
σ_{w1}	coefficient in ω-equation	epistemic	0.3	0.7
σ_{w2}	coefficient in ω-equation	epistemic	0.7	1.0

IV. Uncertainty Quantification and Validation Approach

This section outlines the uncertainty quantification and validation approach used in this study. For the current study, both epistemic and aleatory uncertainties are considered. To accommodate mixed uncertainties, this work used a second-order probability analysis approach which was developed by Eldred and Swiler [29]. To handle the computational burden of this type of approach, non-intrusive polynomial chaos was used as an efficient and accurate means of propagating the uncertainty through the computational model. The first sub-section will describe the surrogate-based approach, and the subsequent sub-section will describe the validation methodology that was used to assess the model discrepancy between the experimental and computational results.

A. Non-intrusive Polynomial Chaos

Polynomial chaos expansion (PCE) is a way of representing a quantity of interest as a function of random variables using a polynomial expansion [6]. The polynomial expansion gives a spectral representation of the uncertainty that can represent the response value as a linear combination of orthogonal stochastic or basis functions, Ψ_i, and suitable coefficients, a_i, as seen in Eq. (3).

$$Y(\mathbf{D}, \xi) = \sum_{i=0}^{\infty} a_i(\mathbf{D})\Psi_i(\xi) \tag{3}$$

Here, $\mathbf{D}$ represents the deterministic variables, and ξ are n independent, standard normal variables. The basis functions of each random variable are represented by an orthogonal polynomial of order q that is determined using the Askey key [6] and is dependent on the distribution of each variable. For practical applications, Eq. (3) must be truncated to a limited number of basis functions, N_t, which leads to Eq. (4).

$$Y(\mathbf{D}, \xi) \approx \sum_{i=0}^{N_t-1} a_i(\mathbf{D})\Psi_i(\xi) \tag{4}$$

To form a complete basis, the number of terms, N_t, can be determined by Eq (5).

$$N_t = \frac{(n+q)!}{n!q!} \tag{5}$$

Further details on polynomial chaos theory can be seen throughout the literature [30–33].

To obtain a PCE model of the form of Eq. (4), the coefficients a_i must be computed. Here, a point-collocation non-intrusive polynomial chaos (NIPC) method was used due to the ease of implementation with black-box functions. This method has also been used extensively in aerospace applications for improved computational efficiency over other spectral based approaches [34–39]. The point-collocation NIPC method starts by computing coefficients using a least squares problem. Given N_t samples of the random variable ξ_k for $k = 1, \ldots, N_t$, the corresponding basis functions, $\Psi_i(\xi_k)$, and the stochastic process, $Y(\mathbf{D}, \xi_k)$, given by Eq. (4), was used to find a suitable linear system as shown in Eq. (6).

$$\begin{pmatrix} Y(\mathbf{D}, \xi_0) \\ \vdots \\ Y(\mathbf{D}, \xi_{N_t}) \end{pmatrix} = \begin{pmatrix} \Psi_0(\xi_0) & \cdots & \Psi_{N_t}(\xi_0) \\ \vdots & \ddots & \vdots \\ \Psi_0(\xi_{N_t}) & \cdots & \Psi_{N_t}(\xi_{N_t}) \end{pmatrix} \begin{pmatrix} a_0 \\ \vdots \\ a_{N_t} \end{pmatrix} \tag{6}$$

For this system, N_t is the minimum number of required samples. If there are more samples, the system in Eq. (6) is over-determined and can be solved as a least squares problem [40]. The number of samples required beyond the minimum required is known as the over sampling ratio (OSR). The number of collocation points is determined by multiplying Eq. (5) by the OSR. For the work here, an OSR of 2 was used to compute a robust solution and to prevent overfitting as shown in Hosder et al. [38].

B. Configuration Study Uncertainty Quantification Approach

Performing uncertainty quantification on each configuration in the geometrical space would be highly computationally expensive. To mitigate the computational burden, this work takes a conservative approach to estimate the lift, drag, and pitching moment coefficient uncertainty for each configuration. This approach used the turbulence parameter plus grid uncertainty found in each configuration that is circled in Table 4 at the nominal wind tunnel conditions.

The second-order expansion surrogate models were used to quantify the impact of turbulence model closure coefficient uncertainty in the lift, drag, and moment coefficient. For a second-order surrogate model, with three uncertain parameters in the turbulence model, $N_t = 30$ CFD runs with each turbulence model combination were performed. The uncertainty was then propagated through the surrogate models for each coefficient using Monte Carlo sampling with 10,000 samples, which was found to be sufficient to converge the epistemic bounds of the uncertainty.

The percent differences of the lower and upper bounds of the uncertainty (model and grid uncertainty) from the nominal VULCAN-CFD cases for lift, drag, and moment coefficients, which are represented by Eqs. (7) and (8) for the upper and lower uncertainty and are listed in Table 7, were used.

$$U^{upper}_{C_i,m} = \begin{cases} \left| \dfrac{C^{upper,Vulcan}_{i,m}(1+U^g_{C_i}) - C^{nominal,Vulcan}_i}{C^{nominal,Vulcan}_i} \right| & \text{if } C^{upper}_{i,m} > 0 \\ \left| \dfrac{C^{upper,Vulcan}_{i,m}(1-U^g_{C_i}) - C^{nominal,Vulcan}_i}{C^{nominal,Vulcan}_i} \right| & \text{else} \end{cases} \tag{7}$$

and

$$U^{lower}_{C_i,m} = \begin{cases} \left| \dfrac{C^{lower,Vulcan}_{i,m}(1-U^g_{C_i}) - C^{nominal,Vulcan}_i}{C^{nominal,Vulcan}_i} \right| & \text{if } C^{lower}_{i,m} > 0 \\ \left| \dfrac{C^{lower,Vulcan}_{i,m}(1+U^g_{C_i}) - C^{nominal,Vulcan}_i}{C^{nominal,Vulcan}_i} \right| & \text{else} \end{cases} \tag{8}$$

Here, $C^{lower}_{i,m}$ is the lower 95% coefficient uncertainty bound found in the UQ study, $C^{upper}_{i,m}$ is the upper 95% uncertainty bound found in the UQ study, and $C^{nominal}_i$ is the force coefficient calculated using VULCAN-CFD at boundary conditions stated in Table 4 with $i \in \{L, M, D\}$ and $m \in \{\text{SA,SST}\}$. Given that the models that were run for the full UQ study span the design space, the approach here assumed that the true combined turbulence parameter and grid uncertainty will lie within the uncertainties listed in Table 7. Therefore, the approach conservatively assumed that the maximum uncertainty discrepancy for each lower and upper bound on each coefficient will suffice for the lower and upper combined grid and turbulence parameter uncertainty bounds for each configuration not used in the UQ study. Note that the moment coefficient has a larger percentage uncertainty due to the values being close to zero, with the magnitudes being on the order of 10^{-2} or smaller.

To construct a predictive model of the uncertainty bounds, a significantly larger amount of CFD analysis would be required. Since this work focuses on developing the least computationally expensive strategy for UQ on the full

Table 7 Combined uncertainty values calculated using Eqs. (7) and (8)

	Configuration							
	1	8	10	13	19	22	25	33
$U^{upper}_{C_L,SA}$	2.41%	2.53%	2.70%	2.79%	2.58%	2.09%	2.47%	2.50%
$U^{upper}_{C_D,SA}$	2.09%	1.31%	2.39%	2.46%	1.19%	1.26%	3.84%	2.41%
$U^{upper}_{C_M,SA}$	17.87%	18.47%	19.30%	20.02%	17.98%	17.14%	22.63%	19.05%
$U^{lower}_{C_L,SA}$	2.45%	2.45%	2.79%	2.50%	2.70%	2.80%	6.13%	2.50%
$U^{lower}_{C_D,SA}$	2.27%	1.34%	2.28%	2.94%	1.27%	1.99%	2.66%	1.49%
$U^{lower}_{C_M,SA}$	17.8%	18.65%	18.52%	19.79%	17.84%	18.41%	19.26%	16.78%
$U^{upper}_{C_L,SST}$	2.46%	2.60%	2.54%	2.65%	2.85%	2.82%	1.77%	2.85%
$U^{upper}_{C_D,SST}$	2.42%	1.59%	4.14%	3.20%	1.85%	2.42%	4.31%	2.88%
$U^{upper}_{C_M,SST}$	17.85%	20.28%	20.74%	20.86%	18.14%	18.10%	19.28%	21.03%
$U^{lower}_{C_L,SST}$	2.60%	2.64%	2.61%	2.28%	3.02%	3.50%	3.70%	2.67%
$U^{lower}_{C_D,SST}$	2.50%	1.88%	2.88%	4.24%	2.68%	3.07%	4.58%	2.73%
$U^{lower}_{C_M,SST}$	17.97%	20.74%	20.89%	19.47%	18.02%	18.29%	18.08%	21.86%

configuration study, the more conservative option of using maximum uncertainty bounds is taken. The formulation of this uncertainty approach is represented by Eq. (9) and the final combined grid and turbulence parameter uncertainty bounds can be seen in Table 8.

$$U^{upper}_{C_i,m} = \max_{j \in \text{config}} \left(U^{upper}_{C_i,m_j} \right) \quad \text{and} \quad U^{lower}_{C_i,m} = \max_{j \in \text{config}} \left(U^{lower}_{C_i,m_j} \right) \tag{9}$$

Here, config = $\{1, 8, 10, 13, 19, 22, 33\}$, $i \in \{L, M, D\}$, and $m \in \{\text{SA}, \text{SST}\}$.

Table 8 Final combined turbulence and grid parameter uncertainty

	lower uncertainty	upper uncertainty
$U_{C_L,SA}$	6.13%	2.79%
$U_{C_D,SA}$	2.94%	3.84%
$U_{C_M,SA}$	19.79%	22.63%
$U_{C_L,SST}$	3.70%	2.85%
$U_{C_D,SST}$	4.58%	4.31%
$U_{C_M,SST}$	21.86%	21.03%

C. Validation Approach

There are many ways to assess a model for validation, as stated by Oberkampf et al. [41–45]. The area metric that was proposed by Brune et al. [39] was used for this work. The area metric was chosen for its robustness in handling model-form uncertainty, when both epistemic and aleatory uncertainties exist, by considering discrepancy at each probability level.

The area metric used here extends on Oberkampf et al. [46] previous approaches to measure the disagreement between both the upper and lower bounding cumulative distribution functions (CDFs) of the prediction and measurement.The resultants are two metrics, d_L and d_R, for left and right bounding CDFs, respectively, which are shown in Eq. (10).

$$d_L = \int_{-\infty}^{\infty} g_L(x)dx, \quad d_R = \int_{-\infty}^{\infty} g_R(x)dx \tag{10}$$

where,

$$g_L(x) = \begin{cases} 0 & \text{for } x \text{ such that } F_L(x) \geq E_L(x) \\ E_L(x) - F_L(x) & \text{for } x \text{ such that } F_L(x) < E_L(x) \end{cases}$$

and

$$g_R(x) = \begin{cases} 0 & \text{for } x \text{ such that } F_R(x) \leq E_R(x) \\ F_R(x) - E_R(x) & \text{for } x \text{ such that } F_R(x) > E_R(x) \end{cases}$$

Here, F_L and F_R are the left and right simulation CDF, respectively, and E_L and E_R, are the left and right experimental CDF, respectively. The resulting metrics d_L and d_R quantify the evidence for disagreement between both the left and right bounding probability distributions while preserving the range of possible distributions from both the prediction and measurements. With this metric, the amount of epistemic uncertainty in the measurements is now accounted for in the metric values. There is still a possibility that one or both values could be zero. A zero value does not imply the two agree, but rather suggests that there is no evidence for disagreement. The validation metric cannot represent a reduction in epistemic uncertainty of the simulation. The model-form uncertainty is independent of the input epistemic uncertainty and, therefore, is not reducible without calibrating the simulation inputs to the same known measurement inputs. An example of Eq. (10) can be seen in Fig. 4. For more information regarding how this metric is defined, see Brune et al. [47].

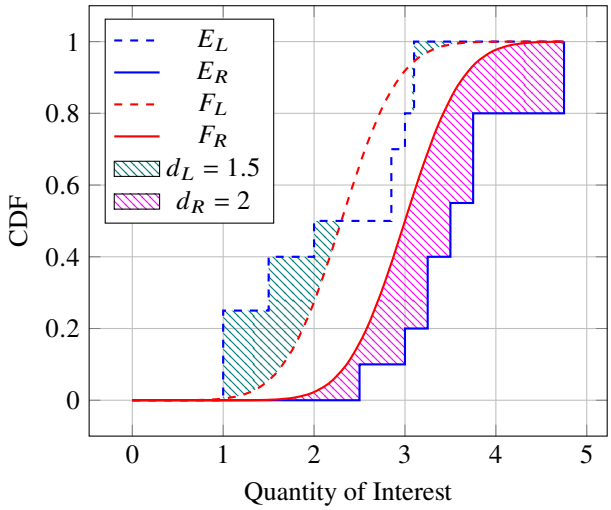

Fig. 4 Example of Eq. (10) where predictions have partial overlap with measurements.

V. Results

This section shows comparisons between the wind tunnel and CFD data. Model-form uncertainty was estimated using the validation methodology described in Section IV.C for the full configuration space, which used the grid uncertainty and turbulence parameter uncertainty from Sections III.A and IV.B, respectively. The model-form uncertainty is then presented for each configuration and for each turbulence model.

A. Analysis and Results

The results here utilize the grid uncertainty estimate from Section III.A, the Cart3D anchoring approach defined in Section III.C, and the combined uncertainty estimate from Section IV.B to capture the model-form uncertainty estimate

on the entire configuration space. The final bounds used in Eq. (10) for F_L and F_R are given by $C_{i,m}^{lower}$ and $C_{i,m}^{upper}$ seen in Eq. (11), respectively.

$$
\begin{aligned}
C_{i,m}^{upper} &= \begin{cases} \underbrace{\left(C_i^{Cart3D} + h_{C_i,m}\left(\frac{R_n}{R_b}, \frac{X_s}{L}, \frac{X_f}{L}, \theta_f, Re, \alpha\right)\right)\left(1 + U_{C_i,m}^{upper}\right)}_{F_R} & \text{if } C_i^{Cart3D} > 0 \\ \underbrace{\left(C_i^{Cart3D} + h_{C_i,m}\left(\frac{R_n}{R_b}, \frac{X_s}{L}, \frac{X_f}{L}, \theta_f, Re, \alpha\right)\right)\left(1 - U_{C_i,m}^{upper}\right)}_{F_R} & \text{else} \end{cases} \\
C_{i,m}^{lower} &= \begin{cases} \underbrace{\left(C_i^{Cart3D} + h_{C_i,m}\left(\frac{R_n}{R_b}, \frac{X_s}{L}, \frac{X_f}{L}, \theta_f, Re, \alpha\right)\right)\left(1 - U_{C_i,m}^{lower}\right)}_{F_L} & \text{if } C_i^{Cart3D} > 0 \\ \underbrace{\left(C_i^{Cart3D} + h_{C_i,m}\left(\frac{R_n}{R_b}, \frac{X_s}{L}, \frac{X_f}{L}, \theta_f, Re, \alpha\right)\right)\left(1 + U_{C_i,m}^{lower}\right)}_{F_L} & \text{else} \end{cases}
\end{aligned}
\tag{11}
$$

Here, $m \in \{\text{SA}, \text{SST}\}$, $i \in \{L, D, M\}$, C_i^{Cart3D} is the coefficient from Cart3D, h_{C_i} is defined in Eq. (1) with $h_{C_L} = h_{C_M} = 0$, $U_{C_i,m}^{lower}$ and $U_{C_i,m}^{upper}$ come from Eq. (9).

After the new lift, drag, and moment coefficient bounds were computed using Eq. (11), the model-form uncertainty was found utilizing Eq. (10). The experimental uncertainty was captured for each configuration applying the methodology described in White et al. [8]. Figure 5 shows examples of the various model-form uncertainty estimates for selected configurations, angles of attack, and coefficients. Note that in Fig. 5b $d_R = d_L = 0$, because the simulation results already cover at least 95% of the data. Observing Fig. 5, when d_R is nonzero then there is underprediction of the CFD distribution compared to the quantity of interest distribution. Similarly, when d_L is nonzero there is overprediction of the CFD distribution compared to the quantity of interest distribution.

Figures 6 show histogram plots of the model-form uncertainty estimates on all the configurations and angles of attack separated out by coefficient for the SA and SST turbulence models. The plots reveal that there is typically an overprediction of drag and lift coefficient for both models. This overprediction of the CFD compared to the experimental results was also seen in configuration 33 which was studied by White et al. [8]. The plots show that for the moment coefficient there is an underprediction for most of the configurations.

When comparing the SA and SST model-form uncertainty estimates for the drag coefficient, the SA model-form uncertainty tends to be larger. The SA turbulence model-form uncertainty being larger is due to the combined turbulence parameter and grid uncertainty for the SST model being larger, as seen in Table 8, which gives a smaller discrepancy between simulation and experiment. For the lift coefficient, the SST model typically shows a larger model-form uncertainty; observing Fig. 6. This is due to the combined grid and turbulence parameter uncertainty being larger for the SA model as shown in Table 8. For the moment coefficient, the SA and SST models show similar trends for d_L and d_R.

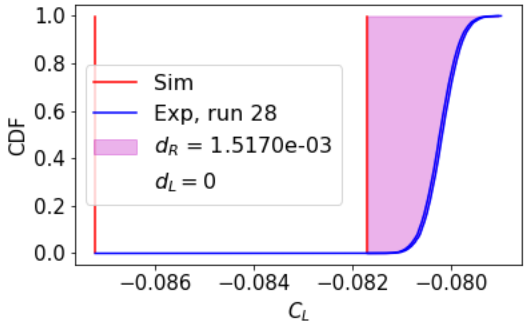

(a) d_L is zero and d_R is nonzero for configuration 21, angle of attack = $-4°$, and SST Model.

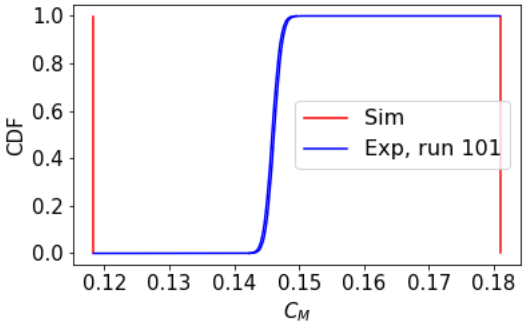

(b) d_L and d_R are both zero for configuration 12, angle of attack = $12°$, and SA model.

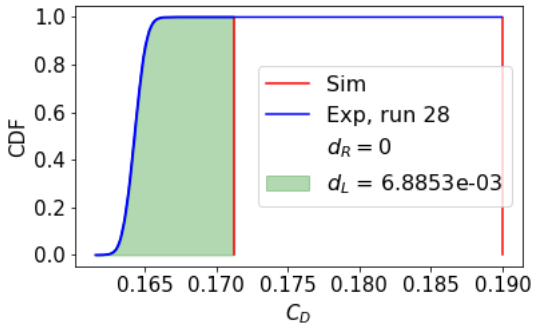

(c) d_L is nonzero and d_R is zero for configuration 21, angle of attack = $4°$, and SST model.

Fig. 5 SA and SST model-form uncertainty estimate examples for various configurations, angles of attack, and coefficients.

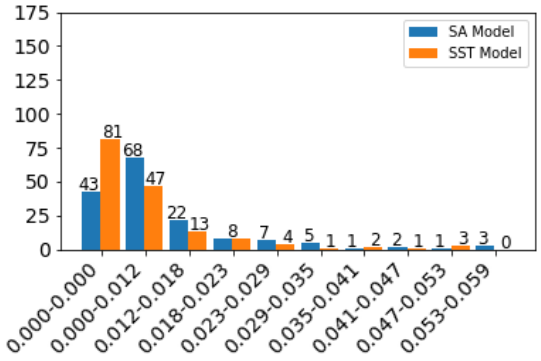

(a) d_L **for the drag coefficient (**$d^{SA}_{C_DL}$ **and** $d^{SST}_{C_DL}$**).**

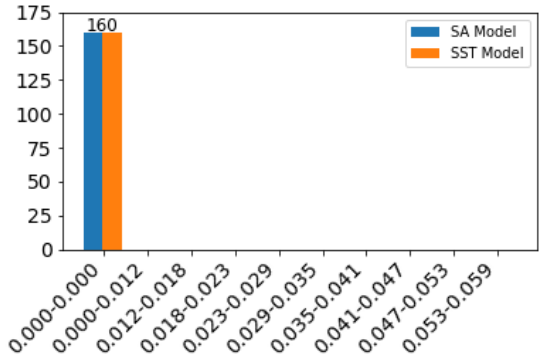

(b) d_R **for the drag coefficient (**$d^{SA}_{C_DR}$ **and** $d^{SST}_{C_DR}$**).**

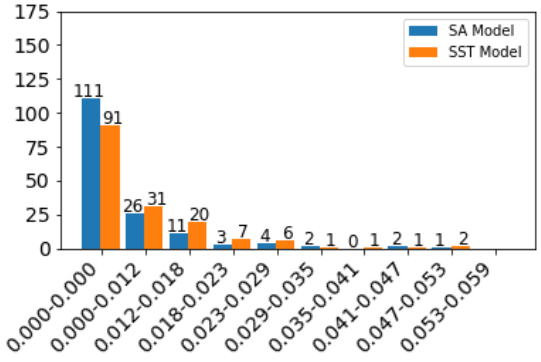

(c) d_L **for the lift coefficient (**$d^{SA}_{C_LL}$ **and** $d^{SST}_{C_LL}$**).**

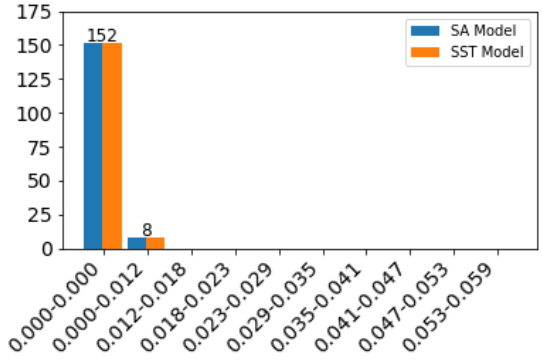

(d) d_R **for the lift coefficient (**$d^{SA}_{C_LR}$ **and** $d^{SST}_{C_LR}$**).**

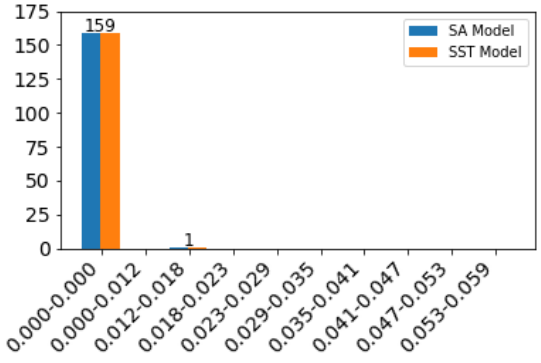

(e) d_L **for the moment coefficient (**$d^{SA}_{C_ML}$ **and** $d^{SST}_{C_ML}$**).**

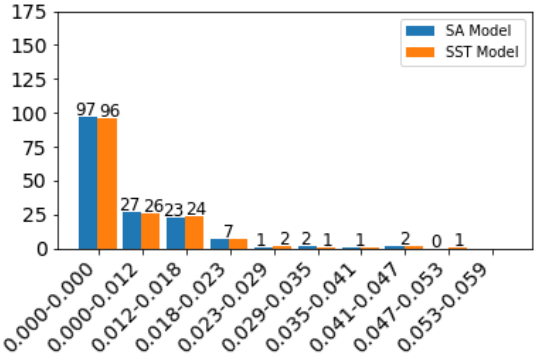

(f) d_R **for the moment coefficient (**$d^{SA}_{C_MR}$ **and** $d^{SST}_{C_MR}$**).**

Fig. 6 Histogram of d_R **and** d_L **for each coefficient using the SA and SST turbulence model.**

Now that the model-form uncertainty estimates have been made, they can be added to the overall uncertainty. Eq. (12) represents what the final added uncertainty is for lift, drag, and moment coefficient.

$$\begin{aligned} C_{C_i,m}^{upper,full} &= C_{C_i,m}^{upper} + d_{C_iR}^{model} \\ C_{C_i,m}^{lower,full} &= C_{C_i,m}^{lower} + d_{C_iL}^{model} \end{aligned} \tag{12}$$

Here, $m \in \{\text{SA}, \text{SST}\}$, $i \in \{L, D, M\}$, $C_{C_i}^{upper}$ and $C_{C_i}^{lower}$ are given by Eq. (11), and $d_{C_iR}^{model}$ and $d_{C_iL}^{model}$ represent the right and left model-form uncertainty estimates found in Fig. 6 for the corresponding coefficient and turbulence model. The layout for the full methodology with how everything is combined can be seen in Fig. 7.

Given the new uncertainty estimates from Eq. (12), a comparison of the percent change from the previous uncertainty compared to the new uncertainty is made. This comparison comes in the form of Eq. (13).

$$\begin{aligned} U_{C_i,m}^{upper,full} &= \frac{C_{C_i,m}^{upper,full} - C_{C_i,m}^{upper}}{|C_{C_i,m}^{upper}| + |C_{C_i,m}^{upper,full}|} \cdot 100 \\ U_{C_i,m}^{lower,full} &= \frac{C_{C_i,m}^{lower,full} - C_{C_i,m}^{lower}}{|C_{C_i,m}^{lower}| + |C_{C_i,m}^{lower,full}|} \cdot 100 \end{aligned} \tag{13}$$

A histogram of all the various percent changes in uncertainty given from Eq. (13) can be seen in Fig.8 for SA and SST models. The percent change uncertainty shows how much the uncertainty bands have changed when incorporating model-form uncertainty into the overall uncertainty estimate. If the simulation models are in good agreement with the experimental data, then there will be a small percent change, otherwise there is a large percent change.

Observing Fig. 8, the moment coefficient tends to have the largest percent change in the uncertainty. This is due to the moment coefficient values for the cone-slice-flap model configurations being typically closer to zero than the other coefficients, with the majority of them being of the order of 10^{-2} or smaller. Due to the moment coefficient values being close to zero, the highest percentage disagreement between experimental and simulation occurs. The lift coefficient showed the second highest percent change, which signifies there was more disagreement between the experimental and simulation data than the drag coefficient.

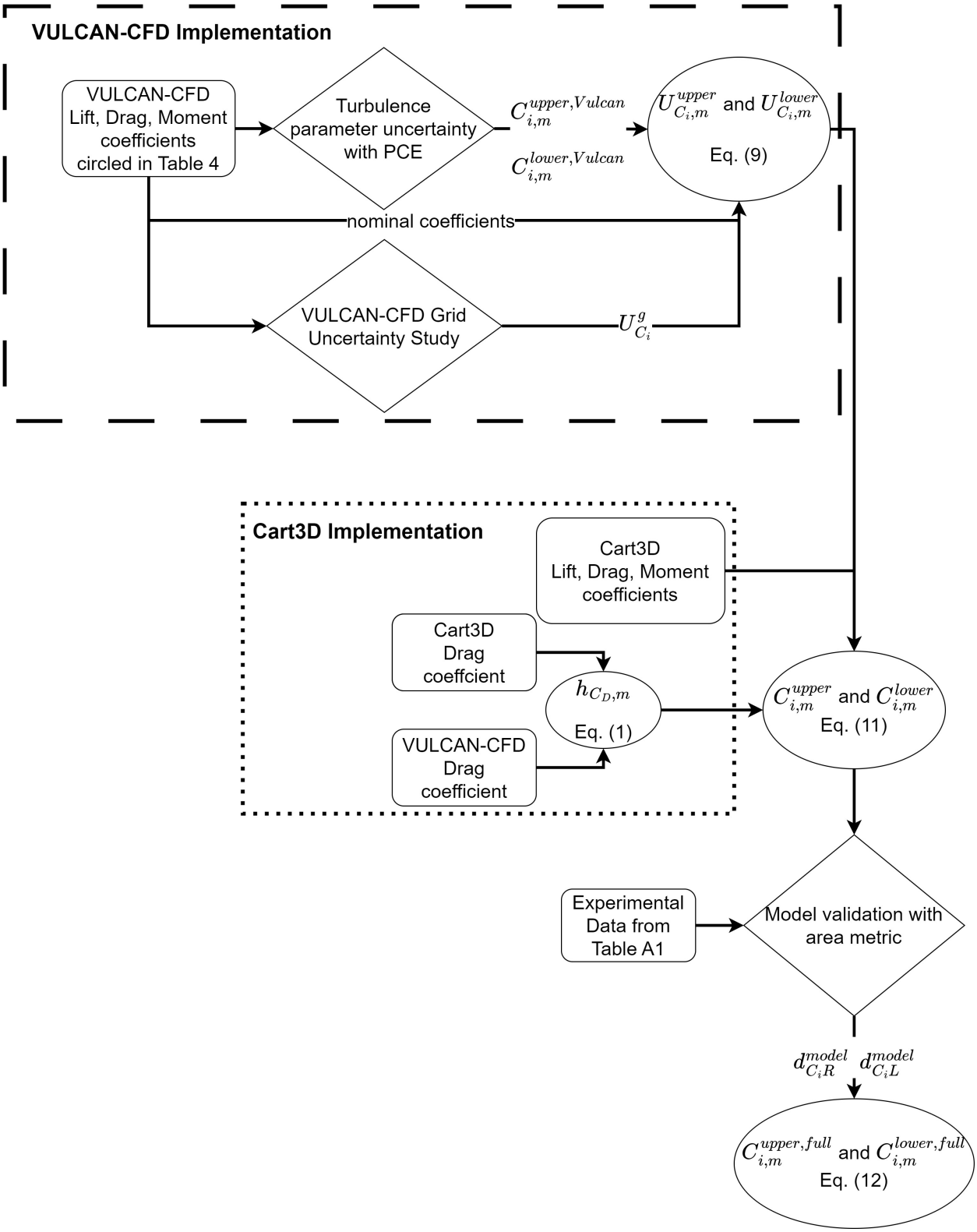

Fig. 7 Methodology layout for combined uncertainty and simulation information.

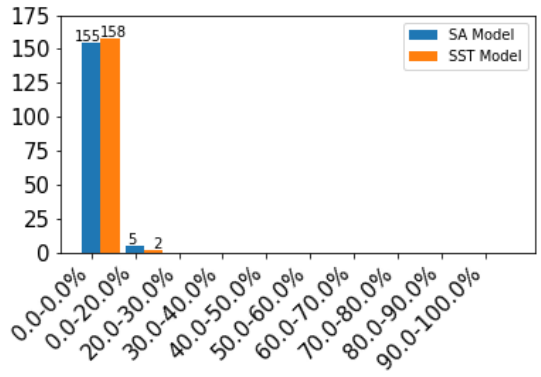

(a) Percent change of the upper uncertainty for the drag coefficient ($U^{lower,full}_{C_D,SA}$ and $U^{lower,full}_{C_D,SST}$).

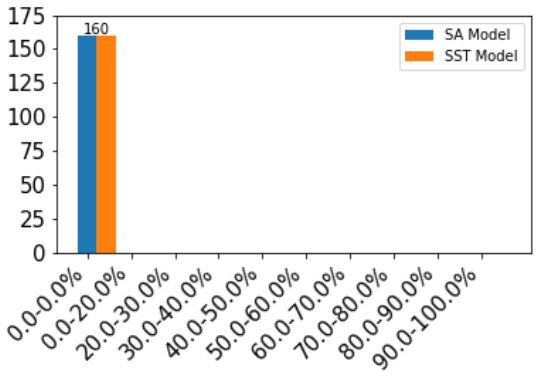

(b) Percent change of the upper uncertainty for the drag coefficient ($U^{upper,full}_{C_D,SA}$ and $U^{upper,full}_{C_D,SST}$).

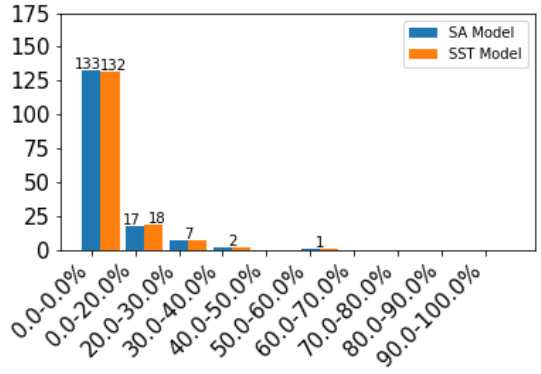

(c) Percent change of the upper uncertainty for lift coefficient ($U^{lower,full}_{C_L,SA}$ and $U^{lower,full}_{C_L,SST}$).

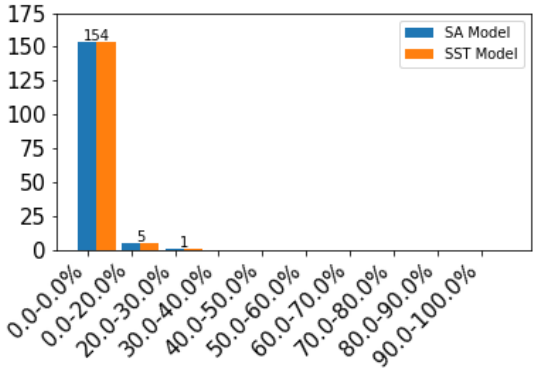

(d) Percent change of the upper uncertainty for lift coefficient ($U^{upper,full}_{C_L,SA}$ and $U^{upper,full}_{C_L,SST}$).

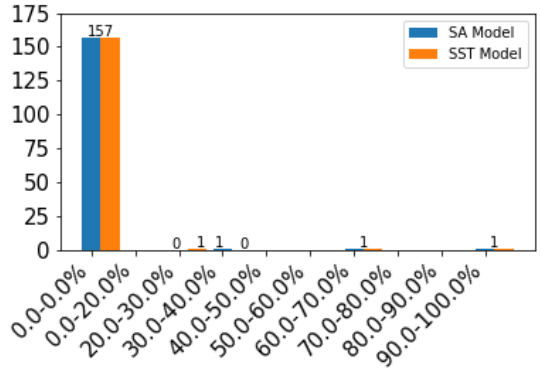

(e) Percent change of the upper uncertainty for the moment coefficient ($U^{lower,full}_{C_M,SA}$ and $U^{lower,full}_{C_M,SST}$).

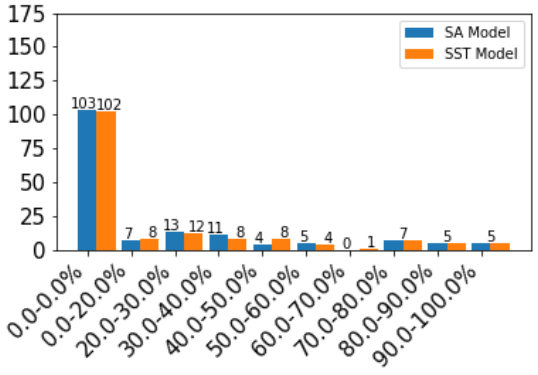

(f) Percent change of the upper uncertainty for the moment coefficient ($U^{upper,full}_{C_M,SA}$ and $U^{upper,full}_{C_M,SST}$).

Fig. 8 Histogram of percent change using Eq. (13) for each coefficient of the SA and SST turbulence model on every configuration.

VI. Concluding Remarks

A computationally efficient methodology for defining the model-form uncertainty for lift, drag, and pitching moment coefficients of a variable cone-slice-flap geometry was presented. For the simulation, turbulence parameter uncertainty was defined for the SA and SST turbulence models. The model-form uncertainty was calculated using a test performed in the 20-inch Mach 6 Tunnel at NASA Langley Research Center and CFD simulations. The analysis accounted for systematic and random error in the experimental measurement, and turbulence parameter and grid uncertainty in the computational fluid dynamic model.

An anchoring approach for the low-fidelity inviscid solver was applied and verified. The low-fidelity solver combined with the anchoring approach was used to define the aerodynamic coefficients for each tested geometric configuration. Then a methodology for classifying the turbulence parameter uncertainty was described and used in combination with the low-fidelity approach to assess uncertainty on the SA and SST turbulence models for each geometrical configuration. After the uncertainty assessment, a model-form uncertainty estimate using a validation area metric was calculated for lift, drag, and pitching moment coefficient for each geometrical configuration at four angles of attack.

The results presented here showed that both turbulence models typically overpredict the drag and lift coefficient and underpredict the pitching moment coefficient. The model-form uncertainty results revealed that each aerodynamic coefficient had a discrepancy from the experimental data on the magnitude of 0.06 or less. The percent change in the overall uncertainty with the model-form uncertainty added was 13.6% or less for the drag coefficient and 57.4% or less for the lift coefficient. For the pitching moment coefficient, the model-form uncertainty percent change was the largest due to its value typically being very close to zero, but in most cases the uncertainty percent change was less than 80%, and ranged up to a percent change of 100%.

The methods and work showcased here can be used for future modelers to provide rationale for a particular turbulence model for a similar hypersonic design. These methods also provide an approach to assess model-form uncertainty when several geometrical parameters are involved and multiple sources of uncertainty. Future work would be to analyze why some of the larger discrepancies exist by performing a high-fidelity analysis such as large eddy simulation or direct numerical simulation.

VII. Acknowledgments

The authors of this paper would like to acknowledge Robert Baurle and Aaron Erb at NASA Langley Research center for their great insight and knowledgeable contributions to this work. The work was funded by the Hypersonic Technology Project under the Aeronautics Research Mission Directorate at NASA.

References

[1] NASA-HDBK-7009, "NASA Handbook for Models and Simulations: An Implementation Guide for NASA-STD-7009A," Standard, NASA, Washington, D.C., May 2019.

[2] Roy, C. J., Oberkampf, W. L., and McWherter-Payne, M. A., "Verification and Validation for Laminar Hypersonic Flowfields, Part 2: Validation," *AIAA Journal*, Vol. 41, No. 10, 2003, pp. 1944–1954. https://doi.org/10.2514/2.1884.

[3] Roy, C. J., McWherter-Payne, M. A., and Oberkampf, W. L., "Verification and Validation for Laminar Hypersonic Flowfields, Part 1: Verification," *AIAA journal*, Vol. 41, No. 10, 2003, pp. 1934–1943. https://doi.org/10.2514/2.1909.

[4] Chynoweth, B. C., Edelman, J., Gray, K., McKiernan, G., and Schneider, S. P., "Measurements in the Boeing/AFOSR Mach-6 Quiet Tunnel on Hypersonic Boundary-Layer Transition," *47th AIAA Fluid Dynamics Conference*, 2017, p. 3632.

[5] Vogel, E., Chynoweth, B. C., Coder, J. G., and Schneider, S. P., "Experimental and Computational Results of a Cone-Slice-Ramp Geometry at Mach 6," *AIAA Aviation 2019 Forum*, 2019, p. 3593. https://doi.org/10.2514/6.2019-3593.

[6] Xiu, D., and Karniadakis, G. E., "The Wiener–Askey Polynomial Chaos for Stochastic Differential Equations," *SIAM Journal on Scientific Computing*, Vol. 24, No. 2, 2002, pp. 619–644. https://doi.org/10.1137/S1064827501387826.

[7] Keyes, J. W., *Force Testing Manual for the Langley 20-inch Mach 6 tunnel*, Vol. 74026, Langley Research Center, 1977.

[8] White, L., West, T. K., Rhode, M. N., Rieken, E., Erb, A. J., Lampenfield, J., and Rodriguez, D., "CFD Validation Study of a Hypersonic Cone-Slice-Flap Configuration," *AIAA Scitech 2021 Forum*, 2021, p. 1074. https://doi.org/10.2514/6.2021-1074.c1.

[9] VULCAN-CFD, *version 7.2.0*, NASA Langley Research Center, Hampton, Virginia, 2022.

[10] Aftosmis, M., Berger, M., and Adomavicius, G., "A Parallel Multilevel Method for Adaptively Refined Cartesian Grids with Embedded Boundaries," *38th Aerospace Sciences Meeting and Exhibit*, 2000, p. 808. https://doi.org/10.2514/6.2000-808.

[11] Spalart, P., and Allmaras, S., "A One-equation Turbulence Model for Aerodynamic Flows," *30th Aerospace Sciences Meeting and Exhibit*, 1992, p. 439. https://doi.org/10.2514/6.1992-439, URL https://doi.org/10.2514/6.1992-439.

[12] Menter, F. R., "Two-equation Eddy-viscosity Turbulence Models for Engineering Applications," *AIAA Journal*, Vol. 32, No. 8, 1994, pp. 1598–1605. https://doi.org/10.2514/3.12149.

[13] Horvath, T., Berry, S., Hollis, B., Singer, B., and Chang, C.-L., "Boundary Layer Transition on Slender Cones in Conventional and Low Disturbance Mach 6 Wind Tunnels," *32nd AIAA Fluid Dynamics Conference and Exhibit*, 2002, p. 2743. https://doi.org/10.2514/6.2002-2743.

[14] Edwards, J. R., "A Low-diffusion Flux-splitting Scheme for Navier-Stokes Calculations," *Computers & Fluids*, Vol. 26, No. 6, 1997, pp. 635–659. https://doi.org/10.1016/S0045-7930(97)00014-5.

[15] Williams, C. K., and Rasmussen, C. E., *Gaussian Processes for Machine Learning*, Vol. 2, MIT Press Cambridge, MA, 2006.

[16] Gramacy, R. B., and Lee, H. K. H., "Bayesian Treed Gaussian Process Models with an Application to Computer Modeling," *Journal of the American Statistical Association*, Vol. 103, No. 483, 2008, pp. 1119–1130. https://doi.org/10.1198/016214508000000689.

[17] Neal, R. M., "Monte Carlo Implementation of Gaussian Process Models for Bayesian Regression and Classification," *ArXiv Preprint Physics/9701026*, 1997.

[18] Ba, S., and Joseph, V. R., "Composite Gaussian Process Models for Emulating Expensive Functions," *The Annals of Applied Statistics*, 2012, pp. 1838–1860. https://doi.org/10.1214/12-AOAS570.

[19] MATLAB, *version 7.10.0 (R2017b)*, The MathWorks Inc., Natick, Massachusetts, 2017.

[20] Cawley, G. C., and Talbot, N. L., "Efficient Leave-one-out Cross-validation of Kernel Fisher Discriminant Classifiers," *Pattern Recognition*, Vol. 36, No. 11, 2003, pp. 2585–2592. https://doi.org/10.1016/S0031-3203(03)00136-5.

[21] Cawley, G. C., "Leave-one-out Cross-validation Based Model Selection Criteria for Weighted LS-SVMs," *The 2006 IEEE International Joint Conference on Neural Network Proceedings*, IEEE, 2006, pp. 1661–1668. https://doi.org/10.1109/IJCNN.2006.246634.

[22] Cawley, G. C., and Talbot, N. L., "Fast Exact Leave-one-out Cross-validation of Sparse Least-squares Support Vector Machines," *Neural Networks*, Vol. 17, No. 10, 2004, pp. 1467–1475. https://doi.org/10.1016/j.neunet.2004.07.002.

[23] Cawley, G. C., and Talbot, N. L., "Efficient Approximate Leave-one-out Cross-validation for Kernel Logistic Regression," *Machine Learning*, Vol. 71, No. 2, 2008, pp. 243–264. https://doi.org/10.1007/s10994-008-5055-9.

[24] Wong, T.-T., "Performance Evaluation of Classification Algorithms by K-fold and Leave-one-out cross Validation," *Pattern Recognition*, Vol. 48, No. 9, 2015, pp. 2839–2846. https://doi.org/10.1016/j.patcog.2015.03.009.

[25] Erb, A. J., and Hosder, S., "Uncertainty Analysis of Turbulence Model Closure Coefficients for Shock Wave-Boundary Layer Interaction Simulations," *2018 AIAA Aerospace Sciences Meeting*, 2018, p. 2077. https://doi.org/10.2514/6.2018-2077.

[26] Erb, A., and Hosder, S., "Uncertainty Analysis of Turbulence Model Closure Coefficients for Wall-Bounded Attached and Separated Flows," *19th AIAA Non-Deterministic Approaches Conference*, 2017, p. 1952. https://doi.org/10.2514/6.2017-1952.

[27] Schaefer, J., Hosder, S., West, T., Rumsey, C., Carlson, J.-R., and Kleb, W., "Uncertainty Quantification of Turbulence Model Closure Coefficients for Transonic Wall-bounded Flows," *AIAA Journal*, Vol. 55, No. 1, 2016, pp. 195–213. https://doi.org/10.2514/1.J054902.

[28] Di Stefano, M., Hosder, S., and Baurle, R., "The Effect of Turbulence Model Uncertainty on Scramjet Isolator Flow Field Analysis," *22nd AIAA International Space Planes and Hypersonics Systems and Technologies Conference*, 2018, p. 5262. https://doi.org/10.2514/6.2018-5262.

[29] Eldred, M. S., and Swiler, L. P., "Efficient Algorithms for Mixed Aleatory-Epistemic Uncertainty Quantification with Application to Radiation-Hardened Electronics. Part 1: Algorithms and Benchmark Results," *Part I: Algorithms and Benchmark Results, Sandia National Laboratories, SAND2009-5805, Albuquerque, NM*, 2009.

[30] Ghanem, R. G., and Spanos, P. D., *Stochastic Finite Elements: A Spectral Approach*, Courier Corporation, 2003. https://doi.org/10.1007/978-1-4612-3094-6.

[31] Eldred, M., and Burkardt, J., "Comparison of Non-Intrusive Polynomial Chaos and Stochastic Collocation Methods for Uncertainty Quantification," *47th AIAA Aerospace Sciences Meeting including the New Horizons Forum and Aerospace Exposition*, 2009, p. 976.

[32] O'Hagan, A., "Polynomial Chaos: A Tutorial and Critique from a Statistician's Perspective," *SIAM/ASA Journal Uncertainty Quantification*, Vol. 20, 2013, pp. 1–20.

[33] Yang, S., Xiong, F., and Wang, F., "Polynomial Chaos Expansion for Probabilistic Uncertainty Propagation," *Uncertainty Quantification and Model Calibration*, 2017, p. 13. https://doi.org/10.5772/intechopen.68484.

[34] Bettis, B., Hosder, S., and Winter, T., "Efficient Uncertainty Quantification in Multidisciplinary Analysis of a Reusable Launch Vehicle," *17th AIAA International Space Planes and Hypersonic Systems and Technologies Conference*, 2011, p. 2393. https://doi.org/10.2514/6.2011-2393.

[35] Hosder, S., Walters, R. W., and Balch, M., "Point-Collocation Nonintrusive Polynomial Chaos Method for Stochastic Computational Fluid Dynamics," *AIAA Journal*, Vol. 48, No. 12, 2010, pp. 2721–2730. https://doi.org/10.2514/1.393893.

[36] Han, D., and Hosder, S., "Inherent and Model-form Uncertainty Analysis for CFD Simulation of Synthetic Jet Actuators," *50th AIAA Aerospace Sciences Meeting including the New Horizons Forum and Aerospace Exposition*, 2012, p. 82. https://doi.org/10.2514/6.2012-82.

[37] West IV, T. K., Hosder, S., and Johnston, C. O., "Multistep Uncertainty Quantification Approach Applied to Hypersonic Reentry Flows," *Journal of Spacecraft and Rockets*, Vol. 51, No. 1, 2013, pp. 296–310. https://doi.org/10.2514/6.2012-82.

[38] Hosder, S., Walters, R., and Balch, M., "Efficient Sampling for Non-intrusive Polynomial Chaos Applications with Multiple Uncertain Input Variables," *48th AIAA/ASME/ASCE/AHS/ASC Structures, Structural Dynamics, and Materials Conference*, 2007, p. 1939. https://doi.org/10.2514/6.2007-1939.

[39] Brune, A. J., West, T. K., and White, L., "Uncertainty Analysis of Probe Surface Predictions for the Hypersonic Material Environmental Test System Facility," *AIAA Scitech 2019 Forum*, 2019, p. 0242. https://doi.org/10.2514/6.2019-0242.

[40] Cheng, H., and Sandu, A., "Collocation Least-squares Polynomial Chaos Method," *Proceedings of the 2010 Spring Simulation Multiconference*, Society for Computer Simulation International, 2010, p. 80. https://doi.org/10.1145/1878537.1878621.

[41] Oberkampf, W. L., and Trucano, T. G., "Verification and Validation in Computational Fluid Dynamics," *Progress in Aerospace Sciences*, Vol. 38, No. 3, 2002, pp. 209–272. https://doi.org/10.1016/S0376-0421(02)00005-2.

[42] Oberkampf, W. L., Trucano, T. G., and Hirsch, C., "Verification, Validation, and Predictive Capability in Computational Engineering and Physics," *Applied Mechanics Reviews*, Vol. 57, No. 5, 2004, pp. 345–384. https://doi.org/10.1115/1.1767847.

[43] Oberkampf, W. L., and Barone, M. F., "Measures of Agreement Between Computation and Experiment: Validation Metrics," *Journal of Computational Physics*, Vol. 217, No. 1, 2006, pp. 5–36. https://doi.org/10.1016/j.jcp.2006.03.037.

[44] Oberkampf, W. L., and Trucano, T. G., "Verification and Validation Benchmarks," *Nuclear Engineering and Design*, Vol. 238, No. 3, 2008, pp. 716–743. https://doi.org/10.1016/j.nucengdes.2007.02.032.

[45] Oberkampf, W. L., and Roy, C. J., *Verification and Validation in Scientific Computing*, Cambridge University Press, 2010. https://doi.org/10.1017/CBO9780511760396.

[46] Oberkampf, W. L., and Ferson, S., "Model Validation Under Both Aleatory and Epistemic Uncertainty," Tech. rep., Sandia National Lab.(SNL-NM), Albuquerque, NM (United States), 2007.

[47] Brune, A. J., West IV, T. K., and White, L. M., "Calibration Probe Uncertainty and Validation for the Hypersonic Material Environmental Test System," *Journal of Thermophysics and Heat Transfer*, Vol. 34, No. 2, 2020, pp. 404–420. https://doi.org/10.2514/1.T5839.

Appendix

Table A1 Experimental run matrix used for CFD validation

Run	Configuration	Avg. RE Number (1/ft)	Avg. Temp. (R)	Avg. Mach
14	33	2600184	863.0629	5.975979
15	33	4014056	861.6114	6.001190
19	21	4017854	863.3080	6.004935
22	20	4087121	860.1499	5.992713
27	25	2760870	865.5565	5.979752
28	21	2618370	862.2260	5.971083
29	33	2609984	861.6857	5.973559
30	33	2082136	865.3221	5.952414
32	33	2068412	865.6804	5.953136
36	10	2623250	862.0067	5.966317
38	30	2099974	864.3319	5.956245
40	18	4047786	863.3194	5.989460
42	6	2611496	863.5742	5.979526
44	4	3994897	866.3972	6.006171
48	19	4011204	864.9235	6.000299
50	24	4057977	864.1663	5.994128
52	33	2593244	863.1498	5.980677
56	15	2625462	864.1682	5.971865
58	12	3996742	866.6559	5.997134
60	11	2609310	867.0585	5.975306
62	8	3997935	871.3356	5.994711
64	22	4064160	865.7501	5.986901
68	7	2592508	868.0978	5.965167
72	32	3334126	866.4547	5.978276
75	27	3495482	866.5538	5.991805
76	33	2597165	864.9561	5.985095
77	1	3954594	872.5978	6.004220
79	13	3996239	865.2612	6.004396
83	29	3822988	867.5079	5.993382
85	10	2617437	861.4600	5.975562
90	33	2564287	875.7828	5.977756
92	16	3891240	875.5039	6.009454
97	23	2571185	875.7253	5.968920
99	11	2559256	878.5598	5.971409
103	14	2594274	871.5671	5.968606
105	3	2558822	878.8524	5.967303
107	11	2561023	873.5087	5.984049
109	10	2524722	879.1732	5.988318
117	5	2547381	879.1761	5.975352
120	33	2512536	879.3820	5.991274